Halo formation at early stage of injection in high-intensity hadron rings

Yoshito Shimosaki and Ken Takayama
Accelerator Laboratory, High Energy Accelerator Research Organization (KEK), Tsukuba, Ibaraki 305-0801, Japan
(Received 8 August 2002; revised manuscript received 7 May 2003; published 22 September 2003)

Halo formation under a nonequilibrium state for a two-dimensional Gaussian beam in a FODO lattice, which is an array of magnets where F is focusing, D is defocusing, and O is the drift space between magnets, was examined in terms of a transition of time-varying nonlinear resonances. Nonlinear resonant-interactions between individual particles and intrinsic beam-core oscillations result in a beam halo. The location of the halo is analytically tractable using canonical equations derived from an isolated resonance Hamiltonian.

DOI: 10.1103/PhysRevE.68.036503 PACS number(s): 29.27.Bd, 41.75.Ak

I. INTRODUCTION

One of the major issues in high-power hadron accelerators is activation of the environment surrounding an accelerator due to beam loss. Beam loss must be reduced to a sufficiently low level to allow hands-on maintenance. In order to produce an acceptable design, it is important to understand the mechanisms of emittance growth and halo formation that result in beam loss.

From this point of view, halo formation has been studied by simulations and theoretical analyses. Especially, particle-in-cell (PIC) simulation codes [1] and analysis using particle-core models (PCM) [2] have greatly facilitated the understanding of space-charge effects. In these studies, a resonant interaction between the individual particles and intrinsic beam-core oscillations has been found to be a driving mechanism of halo formation. However, an analysis using PCM has been made on an equilibrium state, where the rms emittance is constant. The beam property in a nonequilibrium condition, which takes a key role in the resonant interaction of an injected beam, is different from that in equilibrium. Therefore, the PCM could be misleading when a nonequilibrium state is discussed. In addition, it is inaccurate to apply a simulation analysis, such as an fast Fourier transform analysis and a Poincaré map analysis, for a nonequilibrium as that shown in this paper, because these analyses need to track over 100 turns, but the beam distribution varies through the nonequilibrium state in a much shorter time period.

The purpose of this paper is to examine halo formation under a nonequilibrium condition in a circular accelerator. In this context, we have been developing a useful analytic model, which is based on an isolated resonance Hamiltonian (IRH). This model allows us to predict the position and size of the halo as a function of the beam and machine parameters, even in nonequilibrium in terms of time-varying nonlinear resonances.

The organization of this paper is as follows. In Sec. II, the simulation results obtained by the newly developed (2D) two-dimensional simulation code PATRASH (particle tracking in a synchrotron for halo analysis) are presented, where details of the temporal evolution of the particle distribution in phase space are given. In Sec. III, the IRH is analytically derived, while comparing it with the simulation results. In Sec. IV, the time-varying nonlinear resonances that are suggested from the simulation results are theoretically examined based on the IRH. In Sec. V, the obtained results are summarized.

Before proceeding, assumptions concerning the calculations and the example discussed here are noted as follows. The calculations were carried out for 2D mismatched beams with a Gaussian distribution in a typical FODO lattice. Most of the beam/machine parameters are taken from the 12-GeV proton synchrotron of the High Energy Accelerator Research Organization (KEK-PS), where the injection energy is 500 MeV and the circumference is 340 m. No external nonlinear fields, except for space-charge originated fields, were included in the present calculations. In order to manifest a key role of the space-charge effects in halo formation, acceleration was not taken into account and the momentum spread was assumed to be 0%. The combination of bare tunes (ν_x, ν_y) chosen in the present study was close to the operational parameters [$A(7.123,5.229)$ and $B(7.203,5.229)$]. In the case of A, a structure resonance due to a space-charge effect in the horizontal direction has been pointed out in past simulation results, but no resonance was shown in the case of B [3].

II. TEMPORAL EVOLUTION OF THE PARTICLE DISTRIBUTION AFFECTED BY NONLINEAR SPACE-CHARGE FIELDS

In order to delineate the halo-formation mechanisms in a typical FODO lattice, a 2D simulation code PATRASH has been developed [3]. The electric field originating from the space charge is calculated by the hybrid tree code method. PIC-style charge is assigned in the dense core region in a way similar to that in Ref. [4]. Then, the tree code method [5] is applied over the total region of interest. The effects of the image charge are ignored. The space-charge forces are included as δ-function-like kicks in orbit tracking. The longitudinal step size was chosen to be 10 cm, which gave sufficient saturation in the calculation results as a function of the step size. PATRASH'S results were compared with the results of ACCSIM and SIMPSONS [6], which have been independently developed and widely employed for particle tracking in high-intensity hadron rings. The same beam parameters and machine conditions were assumed for this benchmark test. These results have been confirmed to be fairly in agreement with each other, as shown in Fig. 1 [6].

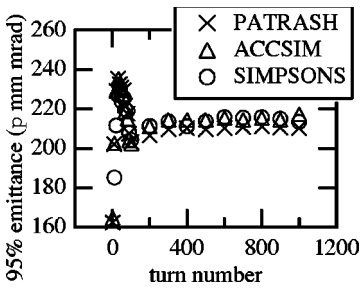

FIG. 1. Comparison between PATRASH, ACCSIM, and SIMPSONS in the horizontal direction.

The simulations were carried out by PATRASH for 2D mismatched beams with the Gaussian distribution for both cases of *A* and *B*. The initial phase-space projections of a mismatched beam are shown in Fig. 2, which were chosen from the actual result observed on the KEK 500-MeV beam-transport line. The footprints on the tune diagram for 200 sampled particles are shown in Fig. 3. The maximum incoherent tune shifts were 0.25 in the horizontal plane and 0.45 in the vertical plane.

The rms emittance growth is shown in Fig. 4. The horizontal and vertical rms emittances in case *B* quickly grew to arrive in the equilibrium state after 5 turns. The vertical rms emittance in case *A* also quickly grew to arrive in equilibrium. On the other hand, the growth of the horizontal rms emittance showed a quite different feature; it continued to grow until 40 turns.

The phase-space projections in the horizontal direction are shown in Figs. 5 and 6, where the particle distribution stays in the nonequilibrium state. In case *A*, the growth of the four characteristic areas is notable, which are identified as the resonance islands (discussed in the following section). Since no nonlinear magnet components were included in these calculations, this nonlinear resonance is apparently driven by nonlinear space-charge self-fields. Particles, whose horizontal depressed tune closes to 7, experienced space-charge fields which oscillated 28 times per 1 turn with the beam-core oscillation due to the 28 FODO cells in KEK-PS. In case *B*, no nonlinear resonances are found in Fig. 6 but, rather, the growth of the filamentation can be recognized.

The time-varying horizontal rms beam sizes in the nonequilibrium state in case *A* are shown in Fig. 7. During the initial few turns, the beam core oscillated with a frequency almost two times higher than the bare tune in cases *A* and *B*. This is simply tumbling in phase space due to mismatching. Beyond the 5th turn, the mismatching oscillation disappeared and the beam core oscillated 28 times per 1 turn.

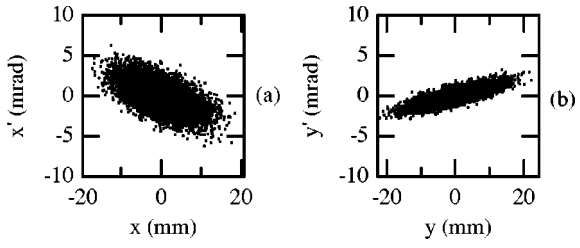

FIG. 2. Initial phase-space maps: (a) horizontal and (b) vertical.

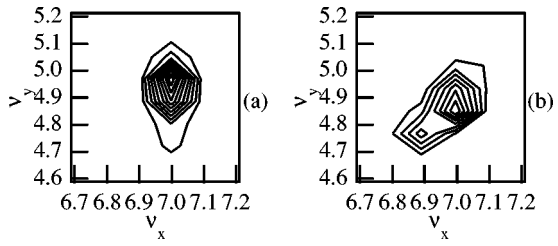

FIG. 3. Tune diagrams: (a) case *A* and (b) case *B*.

The horizontal beam distributions in the nonequilibrium state in case *A* are shown in Fig. 8. The beam distribution remained Gaussian throughout the initial 10 turns in cases *A* and *B*. Beyond this period, the beam distribution for case *A* drastically changed from Gaussian, as shown in Fig. 9.

The simulation results through a transient state clearly indicate that the beam-core oscillation, which drives the halo formation by the parametric nonlinear resonance caused by coupling with the betatron oscillation of an individual particle, is dominated by a combination of mismatching and the lattice structure, and then with the lattice structure alone. However, the simulation results cannot clearly indicate what phenomena occur through this transient state and what mechanism can drive the phenomena through this transient condition.

III. FORMALISM OF AN ISOLATED RESONANCE HAMILTONIAN FOR A GAUSSIAN BEAM

In the early stage of the nonequilibrium state, the whole view of the time dependent process seems to be observed by using snapshots of the first-order Hamiltonian turn by turn. Therefore, the fully analytic approach to explain the simulation results is developed. The PATRASH'S results indicated that the Gaussian distribution is kept within the first 10 turns as shown in Fig. 8. Therefore, it was assumed that the distribution remains Gaussian under nonequilibrium state. The space-charge potential Φ generated by a beam with the Gaussian distribution is written in the form of a Taylor expansion:

$$\Phi(x,y;s)=\frac{eN}{4\pi\epsilon_0}\sum_{n=1}^{\infty}\frac{(-1)^n}{n!}\sum_{r=0}^{n}\binom{n}{r}f_{n,r}(s)x^{2(n-r)}y^{2r}, \tag{1}$$

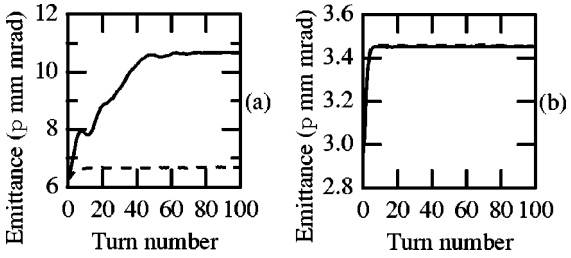

FIG. 4. RMS emittance growth in (a) the horizontal plane and (b) the vertical plane. The solid line is case *A* and the dashed line is case *B*.

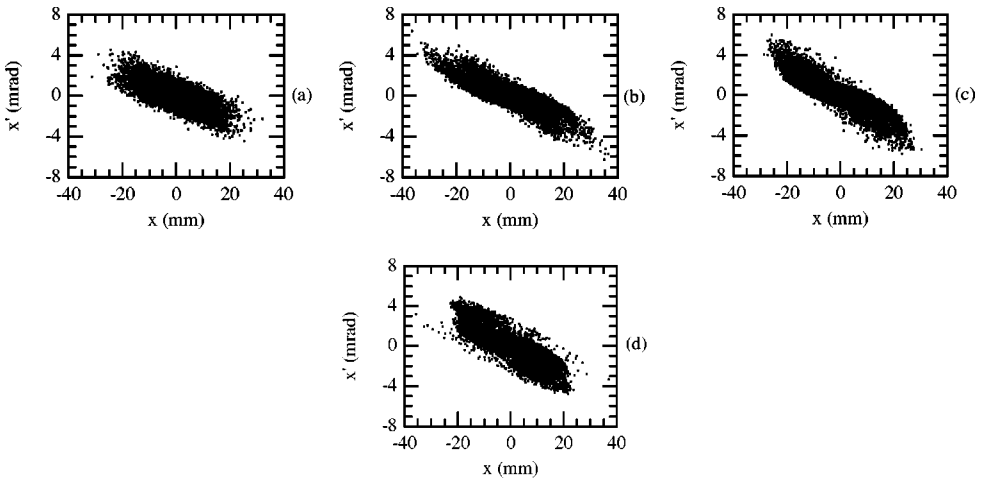

FIG. 5. Phase-space projections at (a) 1st turn, (b) 3rd turn, (c) 5th turn, and (d) 7th turn in case *A*.

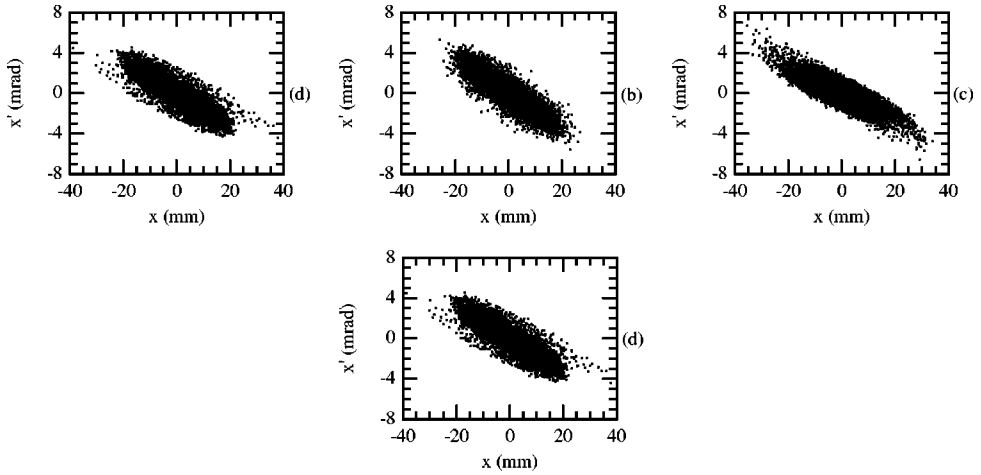

FIG. 6. Phase-space projections at (a) 1st turn, (b) 3rd turn, (c) 5th turn, and (d) 7th turn in case *B*.

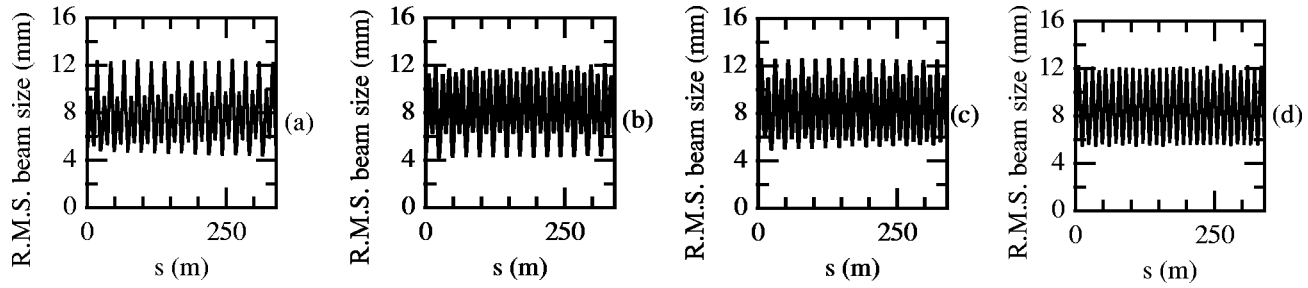

FIG. 7. Time-varying rms beam sizes at (a) 1st turn, (b) 3rd turn, (c) 5th turn, and (d) 7th turn in the horizontal direction. Case *A*.

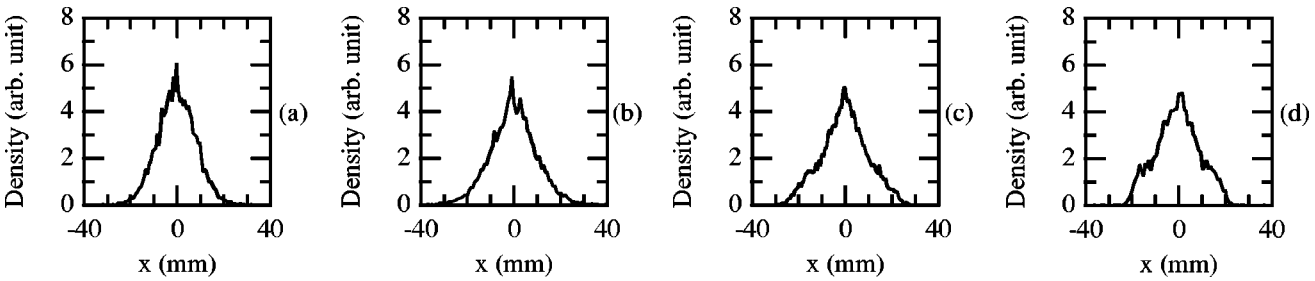

FIG. 8. Beam distribution at (a) 1st turn, (b) 3rd turn, (c) 5th turn, and (d) 7th turn in case *A*.

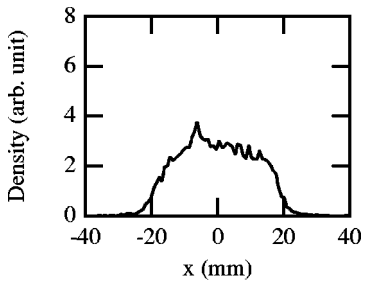

FIG. 9. Beam distribution after 100th turn in case *A*.

$$f_{n,r}(s)=\int_0^\infty \frac{dt}{\{t+2\sigma_x(s)^2\}^{n-r+(1/2)}\{t+2\sigma_y(s)^2\}^{r+(1/2)}},$$

where N is the total number of particles per unit length, ϵ_0 is the permittivity, and σ_x and σ_y are the horizontal and vertical rms beam sizes, respectively. The Hamiltonian describing the betatron oscillation perturbed by the space-charge effects is given in the form

$$H(x,y,p_x,p_y;s)=H_0(x,y,p_x,p_y;s)+\frac{e}{\gamma^2 pv}\Phi(x,y;s),$$

where H_0 is the unperturbed Hamiltonian; γ, p, and v are the relativistic mass factor, the momentum, and the velocity of the on-momentum particle, respectively. By introducing action-angle variables (ψ_x,ψ_y,I_x,I_y) and an independent variable $\theta=s/R_0$ [7], where $x=\sqrt{2\beta_x I_x}\cos(\psi_x+\psi_{0,x})$, $y=\sqrt{2\beta_y I_y}\cos(\psi_y+\psi_{0,y})$, R_0 is the averaged orbit radius, β_x and β_y are Twiss parameters, and $\psi_{0,x}$ and $\psi_{0,y}$ are the flutters of the betatron phase with respect to the averaged phase advance of the unperturbed betatron oscillation, the Hamiltonian is rewritten as

$$H(\psi_x,\psi_y,I_x,I_y;\theta)=\nu_x I_x+\nu_y I_y+\frac{eR_0}{\gamma^2 pv}\Phi(\psi_x,\psi_y,I_x,I_y;\theta). \quad (2)$$

The space-charge potential can be separated into oscillating terms with the angle variable and the other oscillating terms, $g^{(N)}(\theta)$, originating from the flutter, rms beam size, and Twiss parameter. Then, the space-charge potential is written as

$$\begin{aligned}
\Phi(\psi_x,\psi_y,I_x,I_y;\theta)=&\frac{eN}{4\pi\epsilon_0}\sum_{n=1}^{\infty}\frac{(-1)^n}{n!}\frac{1}{2^n}\binom{2n}{n}g_n^{(0)}(\theta)I_x^n+\frac{eN}{2\pi\epsilon_0}\sum_{n=1}^{\infty}\frac{(-1)^n}{n!}\frac{1}{2^n}I_x^n\sum_{l=0}^{n-1}\binom{2n}{l}g_{n,l}^{(1)}(\theta)\cos\{(2n-2l)\psi_x\}\\
&-\frac{eN}{2\pi\epsilon_0}\sum_{n=1}^{\infty}\frac{(-1)^n}{n!}\frac{1}{2^n}I_x^n\sum_{l=0}^{n-1}\binom{2n}{l}g_{n,l}^{(2)}(\theta)\sin\{(2n-2l)\psi_x\}+\frac{eN}{4\pi\epsilon_0}\sum_{n=1}^{\infty}\frac{(-1)^n}{n!}\frac{1}{2^n}\binom{2n}{n}g_n^{(3)}(\theta)I_y^n\\
&+\frac{eN}{2\pi\epsilon_0}\sum_{n=1}^{\infty}\frac{(-1)^n}{n!}\frac{1}{2^n}I_y^n\sum_{l=0}^{n-1}\binom{2n}{l}g_{n,l}^{(4)}(\theta)\cos\{(2n-2l)\psi_y\}\\
&-\frac{eN}{2\pi\epsilon_0}\sum_{n=1}^{\infty}\frac{(-1)^n}{n!}\frac{1}{2^n}I_y^n\sum_{l=0}^{n-1}\binom{2n}{l}g_{n,l}^{(5)}(\theta)\sin\{(2n-2l)\psi_y\}+\frac{eN}{4\pi\epsilon_0}\sum_{n=2}^{\infty}\frac{(-1)^n}{n!}\frac{1}{2^n}\sum_{r=1}^{n-1}\binom{n}{r}\\
&\times\binom{2n-2r}{n-r}\binom{2r}{r}g_n^{(6)}(\theta)I_x^{n-r}I_y^r\\
&+\frac{eN}{2\pi\epsilon_0}\sum_{n=2}^{\infty}\frac{(-1)^n}{n!}\frac{1}{2^n}\sum_{r=1}^{n-1}\binom{n}{r}I_x^{n-r}I_y^r\binom{2r}{r}\sum_{l=0}^{n-r-1}\binom{2n-2r}{l}g_{n,r,l}^{(7)}(\theta)\cos\{(2n-2r-2l)\psi_x\}\\
&-\frac{eN}{2\pi\epsilon_0}\sum_{n=2}^{\infty}\frac{(-1)^n}{n!}\frac{1}{2^n}\sum_{r=1}^{n-1}\binom{n}{r}I_x^{n-r}I_y^r\binom{2r}{r}\sum_{l=0}^{n-r-1}\binom{2n-2r}{l}g_{n,r,l}^{(8)}(\theta)\sin\{(2n-2r-2l)\psi_x\}\\
&+\frac{eN}{2\pi\epsilon_0}\sum_{n=2}^{\infty}\frac{(-1)^n}{n!}\frac{1}{2^n}\sum_{r=1}^{n-1}\binom{n}{r}I_x^{n-r}I_y^r\binom{2n-2r}{n-r}\sum_{m=0}^{r-1}\binom{2r}{r}g_{n,r,m}^{(9)}(\theta)\cos\{(2r-2m)\psi_y\}\\
&-\frac{eN}{2\pi\epsilon_0}\sum_{n=2}^{\infty}\frac{(-1)^n}{n!}\frac{1}{2^n}\sum_{r=1}^{n-1}\binom{n}{r}I_x^{n-r}I_y^r\binom{2n-2r}{n-r}\sum_{m=0}^{r-1}\binom{2r}{r}g_{n,r,m}^{(10)}(\theta)\sin\{(2r-2m)\psi_y\}\\
&+\frac{eN}{2\pi\epsilon_0}\sum_{n=2}^{\infty}\frac{(-1)^n}{n!}\frac{1}{2^n}\sum_{r=1}^{n-1}\binom{n}{r}I_x^{n-r}I_y^r\sum_{l=0}^{n-r-1}\sum_{m=0}^{r-1}\binom{2n-2r}{l}\binom{2r}{m}g_{n,r,l,m}^{(11)}(\theta)\cos\{(2n-2r-2l)\psi_x
\end{aligned}$$

$$+(2r-2m)\psi_y\}-\frac{eN}{2\pi\epsilon_0}\sum_{n=2}^{\infty}\frac{(-1)^n}{n!}\frac{1}{2^n}\sum_{r=1}^{n-1}\binom{n}{r}I_x^{n-r}I_y^r\sum_{l=0}^{n-r-1}\sum_{m=0}^{r-1}\binom{2n-2r}{l}\binom{2r}{m}g_{n,r,l,m}^{(12)}(\theta)$$

$$\times\sin\{(2n-2r-2l)\psi_x+(2r-2m)\psi_y\}+\frac{eN}{2\pi\epsilon_0}\sum_{n=2}^{\infty}\frac{(-1)^n}{n!}\frac{1}{2^n}\sum_{r=1}^{n-1}\binom{n}{r}I_x^{n-r}I_y^r\sum_{l=0}^{n-r-1}\sum_{m=0}^{r-1}\binom{2n-2r}{l}$$

$$\times\binom{2r}{m}g_{n,r,l,m}^{(13)}(\theta)\cos\{(2n-2r-2l)\psi_x-(2r-2m)\psi_y\}-\frac{eN}{2\pi\epsilon_0}\sum_{n=2}^{\infty}\frac{(-1)^n}{n!}\frac{1}{2^n}$$

$$\times\sum_{r=1}^{n-1}\binom{n}{r}I_x^{n-r}I_y^r\sum_{l=0}^{n-r-1}\sum_{m=0}^{r-1}\binom{2n-2r}{l}\binom{2r}{m}g_{n,r,l,m}^{(14)}(\theta)\sin\{(2n-2r-2l)\psi_x-(2r-2m)\psi_y\}, \tag{3}$$

where

$$g_n^{(0)}(\theta)=f_{n,0}\beta_x^n,$$

$$g_{n,l}^{(1)}(\theta)=f_{n,0}\beta_x^n\cos\{(2n-2l)\psi_{0,x}\},$$

$$g_{n,l}^{(2)}(\theta)=f_{n,0}\beta_x^n\sin\{(2n-2l)\psi_{0,x}\},$$

$$g_n^{(3)}(\theta)=f_{n,n}\beta_y^n,$$

$$g_{n,l}^{(4)}(\theta)=f_{n,n}\beta_y^n\cos\{(2n-2l)\psi_{0,y}\},$$

$$g_{n,l}^{(5)}(\theta)=f_{n,n}\beta_y^n\sin\{(2n-2l)\psi_{0,y}\},$$

$$g_{n,r}^{(6)}(\theta)=f_{n,r}\beta_x^{n-r}\beta_y^r,$$

$$g_{n,r,l}^{(7)}(\theta)=f_{n,r}\beta_x^{n-r}\beta_y^r\cos\{(2n-2r-2l)\psi_{0,x}\},$$

$$g_{n,r,l}^{(8)}(\theta)=f_{n,r}\beta_x^{n-r}\beta_y^r\sin\{(2n-2r-2l)\psi_{0,x}\},$$

$$g_{n,r,m}^{(9)}(\theta)=f_{n,r}\beta_x^{n-r}\beta_y^r\cos\{(2r-2m)\psi_{0,y}\},$$

$$g_{n,r,m}^{(10)}(\theta)=f_{n,r}\beta_x^{n-r}\beta_y^r\sin\{(2r-2m)\psi_{0,y}\},$$

$$g_{n,r,l,m}^{(11)}(\theta)=f_{n,r}\beta_x^{n-r}\beta_y^r\cos\{(2n-2r-2l)\psi_{0,x}+(2r-2m)\psi_{0,y}\},$$

$$g_{n,r,l,m}^{(12)}(\theta)=f_{n,r}\beta_x^{n-r}\beta_y^r\sin\{(2n-2r-2l)\psi_{0,x}+(2r-2m)\psi_{0,y}\},$$

$$g_{n,r,l,m}^{(13)}(\theta)=f_{n,r}\beta_x^{n-r}\beta_y^r\cos\{(2n-2r-2l)\psi_{0,x}-(2r-2m)\psi_{0,y}\},$$

$$g_{n,r,l,m}^{(14)}(\theta)=f_{n,r}\beta_x^{n-r}\beta_y^r\sin\{(2n-2r-2l)\psi_{0,x}-(2r-2m)\psi_{0,y}\}.$$

Furthermore, $g(N)(\theta)$ is expanded by Fourier series as

$$g^{(N)}(\theta)=\sum_{k=-\infty}^{\infty}G(k)^{(N)}e^{jk\theta}, \tag{4}$$

$$G(k)^{(N)}=\frac{1}{2\pi}\int_0^{2\pi}g^{(N)}(\theta)e^{-jk\theta}d\theta. \tag{5}$$

Then, the oscillating terms in Eq. (3) are described as

$$g^{(N)}(\theta)\cos(A\psi_x+B\psi_y)=\frac{1}{2}\sum_{k=-\infty}^{\infty}G(k)^{(N)}[e^{j(A\psi_x+B\psi_y+k\theta)}+e^{-j(A\psi_x+B\psi_y-k\theta)}],$$

$$g^{(N)}(\theta)\sin(A\psi_x+B\psi_y)=\frac{1}{2j}\sum_{k=-\infty}^{\infty}G(k)^{(N)}[e^{j(A\psi_x+B\psi_y+k\theta)}-e^{-j(A\psi_x+B\psi_y-k\theta)}].$$

The parametric nonlinear resonances between an individual particle and the intrinsic beam-core oscillation are known to be excited when the phase of a particular Fourier term, of which Φ consists, slowly varies with θ. Because the past simulation results have shown nonlinear resonances in the horizontal direction [3], we focus on the lowest slowly oscillating phase $2a\psi_x-b\theta$, where a and b are integers. The other slowly oscillating phases are given by $i(2a\psi_x-b\theta)$, where i is an integer. The IRH is known to be obtained by averaging the Hamiltonian with respect to θ [8]. In this process, rapidly oscillating terms disappear. Details concerning the evaluation are given in the Appendix. Finally, we arrive at the IRH describing the parametric nonlinear resonance between the betatron oscillation and the oscillating space-charge forces,

$$H_{iso}(\Psi_x,I_x,I_y)=\left(\nu_x-\frac{b}{2a}\right)I_x+\frac{eR_0}{\gamma^2pv}\langle\Phi(\Psi_x,I_x,I_y)\rangle, \tag{6}$$

$$\langle \Phi(\Psi_x, I_x, I_y)\rangle = \frac{eN}{4\pi\epsilon_0}\sum_{n=1}^{\infty}\frac{1}{n!}\binom{2n}{n}G(0)_n^{(0)}\left(-\frac{I_x}{2}\right)^n + \frac{eN}{4\pi\epsilon_0}\sum_{n=2}^{\infty}\frac{1}{n!}\sum_{r=1}^{n-1}\binom{n}{r}\binom{2n-2r}{n-r}\binom{2r}{r}G(0)_{n,r}^{(6)}\left(-\frac{I_x}{2}\right)^{n-r}\left(-\frac{I_y}{2}\right)^r$$
$$+\frac{eN}{4\pi\epsilon_0}\sum_{i=1}^{\infty}\sum_{n=ai}^{\infty}\frac{1}{n!}\left(-\frac{I_x}{2}\right)^n\binom{2n}{n-ai}S_1(i,n)\cos(2ai\Psi_x) + \frac{eN}{4\pi\epsilon_0}\sum_{i=1}^{\infty}\sum_{n=ai}^{\infty}\frac{1}{n!}$$
$$\times\left(-\frac{I_x}{2}\right)^n\binom{2n}{n-ai}S_2(i,n)\sin(2ai\Psi_x) + \frac{eN}{4\pi\epsilon_0}\sum_{i=1}^{\infty}\sum_{n=1+ai}^{\infty}\frac{1}{n!}\sum_{r=1}^{n-ai}\binom{n}{r}\binom{2r}{r}\binom{2n-2r}{n-r-ai}\left(-\frac{I_x}{2}\right)^{n-r}$$
$$\times\left(-\frac{I_y}{2}\right)^r S_3(i,n,r)\cos(2ai\Psi_x) + \frac{eN}{4\pi\epsilon_0}\sum_{i=1}^{\infty}\sum_{n=1+ai}^{\infty}\frac{1}{n!}\sum_{r=1}^{n-ai}\binom{n}{r}\binom{2r}{r}\binom{2n-2r}{n-r-ai}\left(-\frac{I_x}{2}\right)^{n-r}$$
$$\times\left(-\frac{I_y}{2}\right)^r S_4(i,n,r)\sin(2ai\Psi_x), \tag{7}$$

where

$$S_1(i,n) = \frac{2}{\pi}\sum_{u=0}^{n-1}a_{n,u}\int_0^{2\pi}h_x^n\left(\frac{\sigma_y}{\sigma_x}\right)^u \times\cos\{i(2a\psi_{0,x}+b\theta)\}d\theta, \tag{8}$$

$$S_2(i,n) = \frac{2}{\pi}\sum_{u=0}^{n-1}a_{n,u}\int_0^{2\pi}h_x^n\left(\frac{\sigma_y}{\sigma_x}\right)^u \times\sin\{i(2a\psi_{0,x}+b\theta)\}d\theta, \tag{9}$$

$$S_3(i,n,r) = \frac{2}{\pi}\sum_{u=0}^{n-2}c_{n,r,u}\int_0^{2\pi}h_x^{n-r}h_{xy}^r\left(\frac{\sigma_y}{\sigma_x}\right)^{u-2r+1} \times\cos\{i(2a\psi_{0,x}+b\theta)\}d\theta, \tag{10}$$

$$S_4(i,n,r) = -\frac{2}{\pi}\sum_{u=0}^{n-2}c_{n,r,u}\int_0^{2\pi}h_x^{n-r}h_{xy}^r\left(\frac{\sigma_y}{\sigma_x}\right)^{u-2r+1} \times\sin\{i(2a\psi_{0,x}+b\theta)\}d\theta, \tag{11}$$

$$G(0)_n^{(0)} = \frac{1}{\pi}\sum_{u=0}^{n-1}a_{n,u}\int_0^{2\pi}h_x^n\left(\frac{\sigma_y}{\sigma_x}\right)^u d\theta, \tag{12}$$

$$G(0)_{n,r}^{(6)} = \frac{1}{\pi}\sum_{u=0}^{n-2}c_{n,r,u}\int_0^{2\pi}h_x^{n-r}h_{xy}^r\left(\frac{\sigma_y}{\sigma_x}\right)^{u-2r+1}d\theta, \tag{13}$$

$$a_{n,0} = (-1)^n\frac{(2n-2)!!}{(2n-1)!!},$$

$$a_{n,2m} = \sum_{u=1}^{2m}\binom{n}{u}(-1)^{u+1}a_{n,2m-u},$$

$$a_{n,2m+1} = \sum_{u=1}^{2m+1}\binom{n}{u}(-1)^{-u+1}a_{n,2m-u+1} + \frac{(-1)^{m-n-1}}{2m+1}\binom{n-1}{m},$$

$$c_{n,r,0} = \frac{(-1)^n}{2r-1},$$

$$c_{n,r,2m} = \sum_{v=0}^{2m-1}c_{n,r,v}\binom{n}{2m-v}(-1)^{-2m+v+1} + \frac{(-1)^{m-n+1}}{2m-2r+1}\binom{n-1}{m},$$

$$c_{n,r,2m-1,m\neq r} = \sum_{v=0}^{2m-2}c_{n,r,v}\binom{n}{2m-v-1}(-1)^{-2m+v},$$

$$c_{n,r,2r-1} = \sum_{v=0}^{2r-2}c_{n,r,v}\binom{n}{2r-v-1}(-1)^{-2r+v} + \sum_{u=0}^{n-1}\frac{(-1)^{u-n}}{2u-2r+1}\binom{n-1}{u},$$

$$h_x(\theta) = -\frac{\beta_x}{2\sigma_x(\sigma_x+\sigma_y)}, \tag{14}$$

$$h_{xy}(\theta) = -\frac{\beta_y}{2\sigma_x(\sigma_x+\sigma_y)}. \tag{15}$$

H_{iso} and I_y in Eq. (6) become constants of motion. In this paper, the position of the resonance islands is chosen as a measure of the relative strength of nonlinear resonances. The position of the resonance island for a structure resonance is given by I_{xmax} and I_{xmin}, which are the maximum and minimum values of the action variable along the trajectory

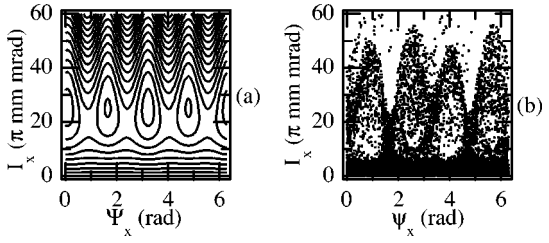

FIG. 10. (a) Contour plot of Hiso and (b) simulation result at the 10th turn.

through the unstable fixed points. The stable and unstable fixed points can be analytically evaluated from the canonical equations.

Equation (7) were numerically calculated as follows. β_x, β_y, $\psi_{0,x}$ and $\psi_{0,y}$ can be given as the definition when the machine parameters such as the tune and the lattice are decided. The informations of σ_x and σ_y for each turn were evaluated by PATRASH, then substituted into Eqs. (8)–(15). It is noted that Eqs. (8)–(15) come from the Fourier series expansion of Eqs. (4) and (5). This means that Eq. (7) is time averaged for one period $(0 \leqslant \theta < 2\pi)$. The nonequilibrium state kept through more than 10 turns as shown in Fig. 4(a), which is clearly longer than the above period. Therefore, the time dependent process under nonequilibrium can be described by the averaged Hamiltonian. Moreover, n_{max}, which is the maximum limit of summation with respect to n in Eq. (1), and I_y were optimized by calculating I_{xmax} and I_{xmin} as functions of n_{max} and I_y, when case A with 8.5×10^{11} particle per bunch beam was assumed. The result saturated around $n_{max}=20$. A larger I_y was found to give smaller resonance islands in the horizontal phase space. In order to estimate the maximum size of the halo, case $I_y=0$ was chosen. A contour plot of H_{iso} is shown in Fig. 10 and compared with the simulation result in case A. Here, $a=1$, $b=14$, and $i_{max}=10$, which is the maximum value of i, were chosen. Furthermore, I_{xmax} and I_{xmin} predicted from H_{iso} were compared with the simulation results. They are also shown in Fig. 11 as functions of the intensity in case A. Both results are in good agreement with each other.

IV. NONLINEAR RESONANCES INDUCED BY COMBINATION OF BEAM-CORE OSCILLATION

As shown in Figs. 4(a) and 5, there are small number of particles with the horizontally large emittance in case A, though the beam distributions still keep the Gaussian form (see Fig. 8) at the early 10 turns. As mentioned at the end of Sec. II, the simulation results cannot clearly indicate what phenomena occur and what mechanism can drive the phenomena by the combination of the beam-core oscillation due to the mismatching and the lattice structure. Therefore, in order to manifest what phenomena occurred by the combination of the beam-core oscillation due to the mismatching and the lattice structure and to predict the position of the halo, the time-varying nonlinear resonances in cases A and B were examined by the IRH (6) for the early 10 turns. By comparing the isolated resonance Hamiltonian of each turn, the phenomena, which are induced by the combination of the beam-core oscillation due to the mismatching and the lattice structure, can be seen clearly.

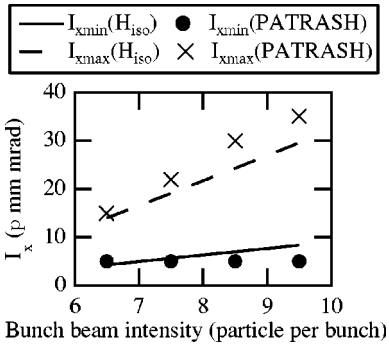

FIG. 11. Intensity dependence of the position of the resonance island (10th turn).

The IRH for case A gives the phase-space structure of the nonlinear resonances, as shown in Fig. 12. The beam core is known to oscillate due to both the lattice structure and the mismatching, as observed in Fig. 7. In Fig. 12(a), b is 14, which is the beam-core oscillation frequency due to the mismatching per 1 turn, as observed in Fig. 7(a). The two resonance islands induced by mismatching are recognized in Fig. 12(a). In Fig. 12(b), b is 28, which corresponds to the periodicity of the lattice structure. The four resonance islands induced due to the lattice structure are confirmed in Fig. 12(b). Including the multiple-beam-core oscillation, the nonlinear resonances caused by the lattice structure and mismatching overlap, as shown in Fig. 12(c).

Next, the IRH for cases A and B was calculated for every turn. The phase-space structures for case A are shown in Fig. 13. The resonance caused by mismatching is dominant at early few turns because the mismatching remains there, as shown in Figs. 7. Furthermore, the nonlinear resonance is switched to the structure resonance, after the decay of mismatching due to the growth of filamentation. Thus, the halo tends to grow in the tune pair of case A. The phase-space structures for case B are shown in Fig. 14. The resonance caused by mismatching is dominant, similar to that of case A. However, because the condition of the structure resonance is not satisfied since the depressed tune is far from 7, the nonlinear resonance is rapidly lost after decay of the mismatching. The particles moving to the resonance island caused by mismatching are thought to be smeared out due to the nonlinear space-charge fields.

The difference in the time-varying nonlinear resonance between cases A and B should be explained by the depressed tune. The depressed tune is given by the time-averaged canonical equation [Eq. (2)], substituting Eq. (3) (see the Appendix) as

$$\left\langle \frac{d\psi_x}{d\theta} \right\rangle = \left\langle \frac{\partial H}{\partial I_x} \right\rangle = \nu_x + \frac{eN}{4\pi\varepsilon_0} \sum_{n=1}^{\infty} \frac{1}{n!} \binom{2n}{n} G(0)_n^{(0)} \left(-\frac{I_x}{2} \right)^n + \frac{eN}{4\pi\varepsilon_0} \sum_{n=2}^{\infty} \frac{1}{n!} \sum_{r=1}^{n-1} \binom{n}{r} \binom{2n-2r}{n-r} \times \binom{2r}{r} G(0)_{n,r}^{(6)} \left(-\frac{I_x}{2} \right)^{n-r} \left(-\frac{I_y}{2} \right)^r . \quad (16)$$

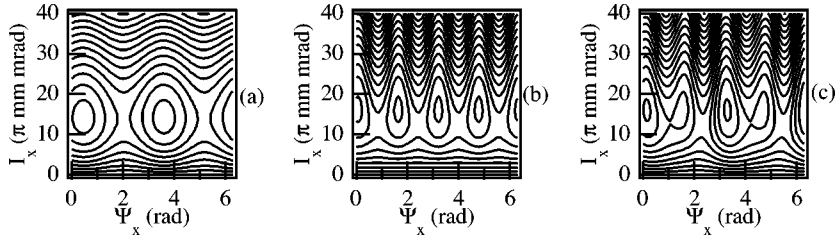

FIG. 12. Phase-space structure of Hiso in case *A*. The nonlinear resonance caused (a) by mismatching ($i_{max}=1$, $a=1$, and $b=14$), (b) by the lattice structure ($i_{max}=1$, $a=2$, and $b=28$) and (c) by the superposition of (a) and (b) ($i_{max}=10$, $a=1$, and $b=14$).

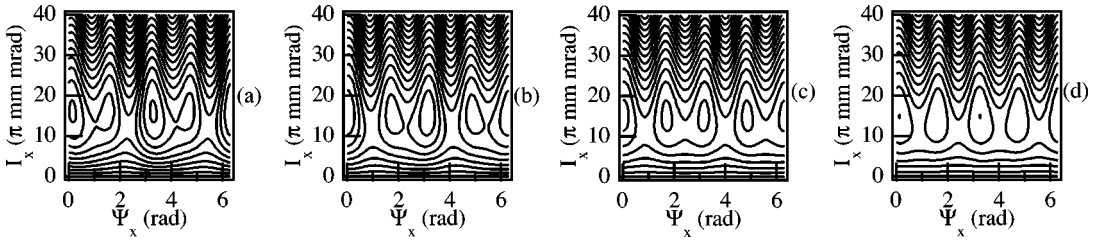

FIG. 13. Time varying of Hiso in case *A*. (a) 1st turn, (b) 3rd turn, (c) 5th turn, and (d) 7th turn. $i_{max}=10$, $a=1$, and $b=14$.

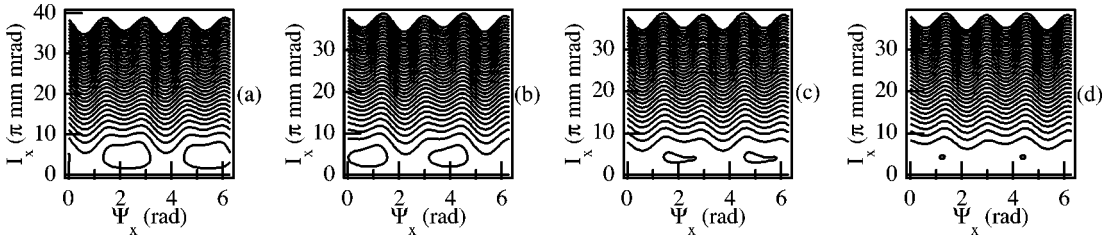

FIG. 14. Time varying of Hiso in case *B*. (a) 1st turn, (b) 3rd turn, (c) 5th turn, and (d) 7th turn. $i_{max}=10$, $a=1$, and $b=14$.

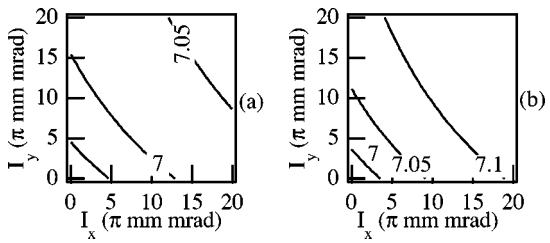

FIG. 15. Depressed tune in cases (a) *A* and (b) *B*.

The depressed tunes of Eq. (16) substituting the rms beam size evaluated by PATRASH are shown in Fig. 15. The resonance line, which is close to 7, is shown in both bare tunes. The resonance island tends to become smaller when the resonance point on the resonance line becomes closer to $I_x=0$. That is, the resonance point becomes closer to $I_x=0$ when I_y becomes larger. Furthermore, the resonance point of case B is closer to $I_x=0$ than for A when $I_y=0$.

V. CONCLUSION

Though the coupling between the nonlinear betatron oscillation of individual particles and the beam-core oscillation seems to drive the halo formation by a mechanism involving the parametric nonlinear resonance, the simulation results cannot clearly prove what phenomena precisely happen in the process and what mechanism can drive these phenomena. An isolated nonlinear resonance theory has been established to understand the whole story, which can consistently explain the phase-space dynamics at the early stage of injection. The isolated nonlinear resonance Hamiltonian has been proved to be a useful tool to estimate the position and size of the halo, which is quite important in a practical sense. It has been concluded that the halo is driven by a time-varying nonlinear resonance excited by the intrinsic beam-core oscillation at the nonequilibrium state.

In the derivation of IRH, the momentum spread is supposed to be 0 for simplicity, but the application of the developed analytic tool is straightforward for on-momentum. While the nonlinear resonances in only the horizontal direction are taken into account in this paper, the vertical and coupling resonances are similarly applied in this theory.

ACKNOWLEDGMENTS

One of the authors (Y.S.) would like to thank K. Ishibashi, K. Maehata, S. Kishiro, T. Toyama, M. Uota, and E. Nakamura for their useful comments throughout this study. He would also like to thank to F. W. Jones for helpful comments concerning PATRASH.

APPENDIX: DERIVATION OF EQ. (6)

We derive the time-averaged space-charge potential of Eq. (3). Here, the horizontal and vertical action variables were assumed to change little in each 1 turn. The time-averaged terms of 5th, 6th and from 10th to 15th in Eq. (3) are all removed because these terms do not include the slowly oscillating term. For the time-averaged 1st, 4th, and 7th terms of Eq. (3), the oscillating terms are removed so that only the constant terms remain. The time-averaged 2nd term of Eq. (3) can be rewritten by using Eq. (4) as

$$
\begin{aligned}
&\left\langle \frac{eN}{2\pi\varepsilon_0}\sum_{n=1}^{\infty}\frac{(-1)^n}{n!}\frac{1}{2^n}I_x^n\sum_{l=0}^{n-1}\binom{2n}{l}g_{n,l}^{(1)}(\theta)\cos\{(2n-2l)\psi_x\}\right\rangle \\
&\quad=\frac{eN}{4\pi\varepsilon_0}\left\langle \sum_{n=1}^{\infty}\frac{(-1)^n}{n!}\frac{1}{2^n}I_x^n\sum_{l=0}^{n-1}\binom{2n}{l}\sum_{k=-\infty}^{\infty}G(k)_{n,l}^{(1)}\cos\{(2n-2l)\psi_x+k\theta\}\right\rangle \\
&\quad\quad+\frac{eN}{4\pi\varepsilon_0}\left\langle \sum_{n=1}^{\infty}\frac{(-1)^n}{n!}\frac{1}{2^n}I_x^n\sum_{l=0}^{n-1}\binom{2n}{l}\sum_{k=-\infty}^{\infty}G(k)_{n,l}^{(1)}\cos\{(2n-2l)\psi_x-k\theta\}\right\rangle \\
&\quad\quad+j\frac{eN}{4\pi\varepsilon_0}\left\langle \sum_{n=1}^{\infty}\frac{(-1)^n}{n!}\frac{1}{2^n}I_x^n\sum_{l=0}^{n-1}\binom{2n}{l}\sum_{k=-\infty}^{\infty}G(k)_{n,l}^{(1)}\sin\{(2n-2l)\psi_x+k\theta\}\right\rangle \\
&\quad\quad-j\frac{eN}{4\pi\varepsilon_0}\left\langle \sum_{n=1}^{\infty}\frac{(-1)^n}{n!}\frac{1}{2^n}I_x^n\sum_{l=0}^{n-1}\binom{2n}{l}\sum_{k=-\infty}^{\infty}G(k)_{n,l}^{(1)}\sin\{(2n-2l)\psi_x-k\theta\}\right\rangle . \qquad \text{(A1)}
\end{aligned}
$$

Because the slowly oscillating phase is assumed as $i(2a\psi_x-b\theta)$ in Sec. III, the terms including $i(2a\psi_x-b\theta)$ are picked up from $(2n-2l)\psi_x\pm k\theta$ in Eq. (A1). Since the other terms are removed by time averaging, Eq. (A1) can be rewritten as

$$
\begin{aligned}
&\left\langle \frac{eN}{2\pi\varepsilon_0}\sum_{n=1}^{\infty}\frac{(-1)^n}{n!}\frac{1}{2^n}I_x^n\sum_{l=0}^{n-1}\binom{2n}{l}g_{n,l}^{(1)}(\theta)\cos\{(2n-2l)\psi_x\}\right\rangle \\
&\quad=\frac{eN}{4\pi\varepsilon_0}\sum_{i=1}^{\infty}\sum_{n=ai}^{\infty}\frac{1}{n!}\left(-\frac{I_x}{2}\right)^n\binom{2n}{l}P(bi)_{n,n-ai}^{(1)}\cos\{i(2a\psi_x-b\theta)\} \\
&\quad\quad+\frac{eN}{4\pi\varepsilon_0}\sum_{i=1}^{\infty}\sum_{n=ai}^{\infty}\frac{1}{n!}\left(-\frac{I_x}{2}\right)^n\binom{2n}{l}Q(bi)_{n,n-ai}^{(1)}\sin\{i(2a\psi_x-b\theta)\},
\end{aligned}
$$

where

$$P(bi)^{(N)}=G(-bi)^{(N)}+G(bi)^{(N)},$$

$$Q(bi)^{(N)}=jG(-bi)^{(N)}-jG(bi)^{(N)}.$$

In the same way, the time-averaged 3rd, 5th, and 6th terms of Eq. (3) are given. Thus, the time-averaged space-charge potential of Eq. (3) is written as

$$\begin{aligned}\langle\Phi(\psi_x,\psi_y,I_x,I_y;\theta)\rangle=&\frac{eN}{4\pi\varepsilon_0}\sum_{n=1}^{\infty}\frac{1}{n!}\binom{2n}{n}G(0)_n^{(0)}\left(-\frac{I_x}{2}\right)^n+\frac{eN}{4\pi\varepsilon_0}\sum_{n=1}^{\infty}\frac{1}{n!}\binom{2n}{n}G(0)_n^{(3)}\left(-\frac{I_y}{2}\right)^n+\frac{eN}{4\pi\varepsilon_0}\sum_{n=2}^{\infty}\frac{1}{n!}\sum_{r=1}^{n-1}\binom{n}{r}\\&\times\binom{2n-2r}{n-r}\binom{2r}{r}G(0)_{n,r}^{(6)}\left(-\frac{I_x}{2}\right)^{n-r}\left(-\frac{I_y}{2}\right)^r+\frac{eN}{4\pi\varepsilon_0}\sum_{i=1}^{\infty}\sum_{n=ai}^{\infty}\frac{1}{n!}\\&\times\left(-\frac{I_x}{2}\right)^n\binom{2n}{n-ai}S_1(i,n)\cos\{i(2a\psi_x-b\theta)\}+\frac{eN}{4\pi\varepsilon_0}\sum_{i=1}^{\infty}\sum_{n=ai}^{\infty}\frac{1}{n!}\\&\times\left(-\frac{I_x}{2}\right)^n\binom{2n}{n-ai}S_2(i,n)\sin\{i(2a\psi_x-b\theta)\}+\frac{eN}{4\pi\varepsilon_0}\sum_{i=1}^{\infty}\sum_{n=1+ai}^{\infty}\frac{1}{n!}\sum_{r=1}^{n-ai}\binom{n}{r}\binom{2r}{r}\binom{2n-2r}{n-r-ai}\\&\times\left(-\frac{I_x}{2}\right)^{n-r}\left(-\frac{I_y}{2}\right)^r S_3(i,n,r)\cos\{i(2a\psi_x-b\theta)\}+\frac{eN}{4\pi\varepsilon_0}\sum_{i=1}^{\infty}\sum_{n=1+ai}^{\infty}\frac{1}{n!}\sum_{r=1}^{n-ai}\binom{n}{r}\binom{2r}{r}\binom{2n-2r}{n-r-ai}\\&\times\left(-\frac{I_x}{2}\right)^{n-r}\left(-\frac{I_y}{2}\right)^r S_4(i,n,r)\sin\{i(2a\psi_x-b\theta)\},\end{aligned}\tag{A2}$$

where

$$S_1(i,n)=P(bi)_{n,n-ai}^{(1)}+Q(bi)_{n,n-ai}^{(2)},\tag{A3}$$

$$S_2(i,n)=-P(bi)_{n,n-ai}^{(2)}+Q(bi)_{n,n-ai}^{(1)},\tag{A4}$$

$$S_3(i,n,r)=P(bi)_{n,r,n-r-ai}^{(7)}+Q(bi)_{n,r,n-r-ai}^{(8)},\tag{A5}$$

$$S_4(i,n,r)=-P(bi)_{n,r,n-r-ai}^{(8)}+Q(bi)_{n,r,n-r-ai}^{(7)}.\tag{A6}$$

$G(0)_n^{(0)}$, $G(3)_n^{(0)}$, $G(6)_n^{(0)}$, and Eqs. (A3)–(A6) can be integrated by using Eq. (5) and

$$\int_0^{\infty}\frac{dt}{(t+a^2)^{n+(1/2)}(t+b^2)^{(1/2)}}=\frac{2(-1)^n}{a^n(b+a)^n}\sum_{u=0}^{n-1}a_{n,u}\left(\frac{b}{a}\right)^u,$$

$$\int_0^{\infty}\frac{dt}{(t+a^2)^{n-r+(1/2)}(t+b^2)^{r+(1/2)}}=\frac{2(-1)^n}{a^n(b+a)^n}\sum_{u=0}^{n-2}c_{n,r,u}t^{u-2r+1}.$$

The time-averaged Hamiltonian of Eq. (2) is given by using Eq. (A2) as

$$\langle H(\psi_x,\psi_y,I_x,I_y;\theta)\rangle=\nu_xI_x+\nu_yI_y+\frac{eR_0}{\gamma^2pv}\langle\Phi(\psi_x,\psi_y,I_x,I_y;\theta)\rangle.\tag{A7}$$

Since $d\psi_y/d\theta=d\langle H\rangle/dI_y=0$, I_y is the constant of motion. Therefore, we remove the 2nd term of Eq. (A2) and the 2nd term of Eq. (A7). Furthermore, since $\langle H\rangle$ is not a constant of the motion, the canonical transformation from (ψ_x,I_x) to $(\Psi_x=\psi_x-b\theta/(2a),I_x)$ is made, where the generating function is $F_2(\psi_x,I_x)=\{\psi_x-b\theta/(2a)\}I_x$. Thus, the isolated resonance Hamiltonian (6) and is obtained.

[1] H. Okamoto and M. Ikegami, Phys. Rev. E **55**, 4694 (1997).
[2] M. Ikegami, Nucl. Instrum. Methods Phys. Res. A **435**, 284 (1999).
[3] Y. Shimosaki and K. Takayama, in *Proceedings of the 7th European Particle Accelerator Conference*, edited by J.-L. Laclare, W. Mitaroff, Ch. Petit-Jean-Genaz, J. Poole, and M. Regler (Austrian Academy of Sciences Press, Vienna, 2000), p. 1330.
[4] F. W. Jones, in *Workshop on Space Charge Physics in High Intensity Hadron Rings, Shelter Island, NY, 1998*, edited by A. U. Luccio and W. T. Weng, AIP Conf. Proc. No. 448 (AIP, Woodbury, NY, 1998), p. 359.
[5] J. Makino, Bull. Jpn. Soc. Ind. Appl. Math. **8**(4), 277 (1998).
[6] K. Takayama *et al.*, in Accelerator Technical Design Report for J-PARC (JAERI/KEK joint project), KEK Report No. 2002-13, JAERI-Tech 2003-044, p. 140 (unpublished).
[7] D. Edwards and M. Syphers, *An Introduction to the Physics of High Energy Accelerators* (Wiley Interscience, New York, 1993).
[8] Y. Shimosaki and K. Takayama, Phys. Rev. E **62**, 2797 (2000).